Theoretical analysis of single-ion anisotropy in d^3 Mott insulators

Xiaoyu Liu,[1] Derek Churchill,[1] and Hae-Young Kee[1,2,*]
[1]*Department of Physics, University of Toronto, Ontario, Canada M5S 1A7*
[2]*Canadian Institute for Advanced Research, CIFAR Program in Quantum Materials, Toronto, Ontario, Canada M5G 1M1*

(Received 27 March 2022; accepted 29 June 2022; published 14 July 2022)

An effective spin model for Mott insulators is determined by the symmetries involved among magnetic sites, electron fillings, and their interactions. Such a spin Hamiltonian offers insight to mechanisms of magnetic orders and magnetic anisotropy beyond the Heisenberg model. For a spin moment S bigger than 1/2, single-ion anisotropy is in principle allowed. However, for d^3 Mott insulators with large cubic crystal field splitting, the single-ion anisotropy is absent within the LS coupling, despite S = 3/2 local moment. On the other hand, preferred magnetic moment directions in d^3 materials have been reported, which calls for a further theoretical investigation. Here we derive the single-ion anisotropy interaction using the strong-coupling perturbation theory. The cubic crystal field splitting including e_g orbitals, trigonal distortions, Hund's coupling, and spin-orbit coupling beyond the LS scheme are taken into account. For compressed distortion, the spin-orbit coupling at magnetic sites can favor either the easy-axis or the easy-plane while that of anions leads to easy-axis anisotropy. We apply the theory on CrX_3 with X = Cl and I, and show the dependence of the single-ion anisotropy on the strength of the spin-orbit couplings of both magnetic and anion sites. Significance of the single-ion anisotropy in ideal two-dimensional magnets is also discussed.

DOI: 10.1103/PhysRevB.106.035122

I. INTRODUCTION

Two-dimensional (2D) magnets have been of great interest in both fundamental and applied research communities due to their intrinsic long-range order (LRO) and potential application in spintronics, data storage, and sensing [1,2]. In particular, recent progresses on 2D materials such as monolayer CrI_3 [3] and bilayer $Cr_2Ge_2Te_6$ [4] have generated intense theoretical and experimental activities to understand and control physical properties via pressure, strain, doping, and/or stacking into heterostructures [5–10]. These 2D materials exhibit paramagnetic (PM) to ferromagnetic (FM) transition at a critical temperature T_c. This immediately implies that their effective spin model is beyond SU(2) symmetric Heisenberg interaction, because there is no LRO in 2D Heisenberg magnets at any finite temperature due to thermal fluctuations, i.e., celebrated Mermin-Wagner theorem [11]. Thus the magnetic anisotropy is crucial for 2D magnets to hold the LRO at finite temperatures. Previous studies showed that such anisotropy includes the single-ion anisotropy (SIA) for spin $\mathbf{S}$ bigger than 1/2, XXZ model [12,13], and/or bond-dependent interactions such as Kitaev and Γ interactions [14,15], as they are allowed by the symmetry of crystal.

While the symmetry is a strong constraint to the effective spin model, it is not sufficient to determine the pinning of magnetic moment direction and the size of spin gap essential for a finite temperature LRO. To access the information beyond the symmetry-allowed terms, the spin Hamiltonian in relation to virtual hoppings between different magnetic sites is necessary. Such a model can be derived using the standard strong coupling expansion theory starting from the multi-orbital Kanamori-Hubbard interaction [16] and treating inter- and intraorbital hoppings as perturbations. It is well established that the magnetic anisotropy including popular bond-dependent Kitaev and Γ interactions originates from the interplay between spin-orbit coupling (SOC), crystal field splitting, as well as Hund's coupling [17–21].

For d^3 Mott insulators such as Cr^{3+}, there are three electrons in six t_{2g} orbitals in the limit when the cubic crystal field splitting is infinite (i.e., ignoring the e_g orbitals). This maps to the half-filled t_{2g} orbitals, where the total spin $\mathbf{S} = \sum_i \mathbf{s}_i = \frac{3}{2}$ and total angular momentum $\mathbf{L} = \sum_i \mathbf{l}_i = 0$ based on the first and second Hund's rule respectively. In this case, the SIA is absent because $\mathbf{L} = 0$ within the LS coupling scheme ($\lambda \mathbf{L} \cdot \mathbf{S}$). This means that the spin anisotropy should come from a finite trigonal crystal splitting and/or beyond the LS coupling, i.e., sum of each atomic SOC, $\xi \sum_i \mathbf{l}_i \cdot \mathbf{s}_i$. In real solid-state materials, there is an additional crystal field splitting from trigonal distortion, as 2D materials are grown on substrates, which is crucial for a finite SIA in addition to SOC. While the above arguments are expected, the analytical expression of SIA for d^3 systems has not been fully explored.

In this paper, we study how the SIA depends on the SOC, crystal field splitting, Hund's coupling, and trigonal distortion in d^3 S = 3/2 systems. We present analytical expressions for SIA in various limits. We find the SIA depends on the relative strength of the cubic crystal field splitting and the Hund's coupling. The easy-axis versus easy-plane direction is determined by the trigonal distortion when the e_g contribution is included, while they work against each other in the large Hund's coupling limit. For a compressed distortion, the SOC

*hykee@physics.utoronto.ca

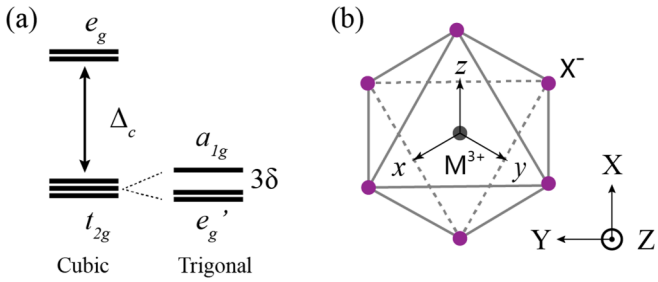

FIG. 1. (a) Crystal field splitting under cubic and trigonal fields. The splitting between a_{1g} and e'_g is 3δ where δ denotes the trigonal field effect defined in Eq. (1). (b) An octahedral cage in MX_3. The local axis (x, y, z) is defined along the octahedral axis. The global axis (X, Y, Z) is defined with Z along the (111) direction in the local coordinate system, perpendicular to the edge-sharing octahedral honeycomb.

at magnetic sites can either favor the easy-plane or -axis depending on the $p-d$ hybridization, while that of anions leads to easy-axis single-ion anisotropy. We hope our result will offer a useful guideline to estimate the SIA and enhance T_c in d^3 systems.

The paper is organized as follows. In Sec. II, we discuss the on-site Hamiltonian and its spectrum under SOC and trigonal distortions. In Sec. III, we discuss the spin model for d^3 S $= 3/2$, and the SIA from the strong-coupling perturbation method. In Sec. IV, we discuss the SIA originated from the p-orbital SOC. In Sec. V, we apply our theory on CrX_3, with X = Cl, I, and show how the total SIA from both the magnetic and anion sites depends on the relative strength of SOC between them. A short summary and discussion are presented in the last section.

II. THE ON-SITE HAMILTONIAN

MX_3 where M a transition metal and X a halide is composed of edge-sharing MX_6 octahedra, forming a 2D honeycomb structure. The octahedral coordination of the MX_6 cages leads to a cubic crystal field splitting (CFS) $H_{\text{cubic}} = \sum_{\alpha\in e_g} \Delta_c\, c^\dagger_\alpha c_\alpha$ on the M site, as shown in Fig. 1(a). Beside the cubic CFS, in van der Waals materials, the octahedral cages are usually trigonally distorted, leading to a further trigonal field splitting δ shown in Fig. 1(a) with

$$H_{\text{trig}} = \begin{pmatrix} 0 & \delta & \delta \\ \delta & 0 & \delta \\ \delta & \delta & 0 \end{pmatrix}. \tag{1}$$

The equation is written in basis (d_{xy}, d_{yz}, d_{zx}), where the x, y, and z are the local axes of the octahedron, as shown in Fig. 1(b). It is equivalent to $H_{\text{trig}} = \delta(2 - 3L_Z^2)$ [22] with L_Z being the angular momentum along the Z direction, which is perpendicular to the 2D honeycomb lattice, as shown in Fig. 1(b). Compression of the octahedral cage prefers $L_Z = 0$, which is generally associated with positive δ.

Since we are interested in the effective spin model of multiorbital Mott insulators, we begin with the Kanamori-Hubbard model [16],

$$\begin{aligned} H_{\text{Coulomb}} = U \sum_\alpha n_{\alpha\uparrow} n_{\alpha\downarrow} + \frac{U'}{2} \sum_{\alpha\neq\beta,\sigma,\sigma'} n_{\alpha\sigma} n_{\beta\sigma'} \\ - \frac{J_H}{2} \sum_{\alpha\neq\beta,\sigma\sigma'} c^\dagger_{\alpha\sigma} c^\dagger_{\beta\sigma'} c_{\beta\sigma} c_{\alpha\sigma'} \\ + J_H \sum_{\alpha\neq\beta} c^\dagger_{\alpha\uparrow} c^\dagger_{\alpha\downarrow} c_{\beta\downarrow} c_{\beta\uparrow}, \end{aligned} \tag{2}$$

where the U and U' are the intra and interorbital Coulomb interactions, J_H is the Hund's coupling. $c^\dagger_{\alpha\sigma}$ and $c_{\alpha\sigma}$ are creation and annihilation operators of α orbital with spin σ. $n_{\alpha\sigma}$ is the density operator.

Here we use the simplified multiorbital model ignoring 3- and 4-orbital interaction terms, which become important when e_g orbitals are not well separated from t_{2g} [23–25]. Since the cubic crystal field splitting is rather large, we expect that the simplified Kanamori Hamiltonian Eq. (2) is a good approximation. We indeed find including 3- and 4-orbital interaction terms, which is denoted by full interaction model in Appendix A, gives small corrections to the SIA.

Without SOC the spins do not have a preferred direction within spin space. To explain the (intrinsic) magnetic anisotropy in MX_3 systems, we include the SOC to entangle the spin and orbitals defined on a lattice. The atomic SOC is given by the summation of the SOC on each electron i,

$$H_{\text{SOC}} = \xi_M \sum_i \mathbf{l}_i \cdot \mathbf{s}_i. \tag{3}$$

Here the $\mathbf{l}_i$ and $\mathbf{s}_i$ are the angular momentum and spin momentum of each electron respectively. The SOC effect can be approximated by $H^{\text{LS}}_{\text{SOC}} = \lambda(L, S)\mathbf{L}\cdot\mathbf{S}$ as discussed earlier, and we will consider the both cases and show how the results of SIA differ between the two approaches.

The total on-site Hamiltonian is the summation of the above terms,

$$H_{\text{tot}} = H_{\text{Coulomb}} + H_{\text{cubic}} + H_{\text{SOC}} + H_{\text{trig}}. \tag{4}$$

When $\Delta_c > U$, the electrons on M^{3+} ions tend to stay on t_{2g} orbitals. When the Hund's coupling is finite, the lowest energy state is described by three electrons in t_{2g} aligned to form S $= 3/2$. The excited states depend on the strength of the cubic CFS Δ_c. When Δ_c is infinite, where e_g orbitals are not taken into account, we will be limited to all excited states within t^3_{2g} configurations. Throughout this paper we will use t^3_{2g} for such a case where e_g states are not considered, while we will use d^3 for three electrons in any d orbitals in excited states. Without SOC and trigonal field splittings, the spectrum of t^3_{2g} is listed in the first part of Table I. The lowest fourfold degenerate states have total spin $S = \frac{3}{2}$ and total angular momentum $L = 0$. The two sets of excited states are 10-fold and sixfold with $L = 2$, $S = \frac{1}{2}$ and $L = 1$, $S = \frac{1}{2}$ respectively.

In the presence of SOC and trigonal field, couplings between the lowest states and the excited states are enabled. Carrying out the numerical calculations for small SOC and trigonal field, the spectrum under this circumstance as a function of δ/ξ_M is shown in Fig. 2(a). When we zoom in

TABLE I. Spectrum. Assume $U' = U - 2J_H$.

Degeneracy	Energy
t_{2g}^3	
4	$3U - 9J_H$
10	$3U - 6J_H$
6	$3U - 4J_H$
$d^3, \Delta_c = 0$	
40	$3U - 9J_H$
70	$3U - 6J_H$
10	$3U - 2J_H$
$d^3, J_H = 0$	
20	$3U$
60	$3U + \Delta_c$
36	$3U + 2\Delta_c$
4	$3U + 3\Delta_c$

to the lowest states, we find the lowest fourfold degenerate $S = \frac{3}{2}$ states split into two doublets with $S_Z = \pm\frac{1}{2}$ (blue) and $S_Z = \pm\frac{3}{2}$ (red), as shown in Fig. 2(b). For small positive δ (corresponding to compression along Z direction), $S_Z = \pm\frac{1}{2}$ doublets have lower energy, indicating a preference of spin moment lying in-plane. Around $\delta \approx \xi_M$ for a positive δ, the two doublets cross again and $S_Z = \pm\frac{3}{2}$ are preferred at large positive δ, consistent with the earlier numerical result found in [26].

The above finding is under the assumption of t_{2g}^3 configuration. In real materials, excited states can have electrons in any d orbitals including the e_g orbitals, i.e., d^3 configuration. The exact spectrum of d^3 configuration cannot be obtained analytically, as the Hund's coupling and the cubic CFS do not commute with each other. Thus we present d^3 spectrum under two extreme conditions, as shown in the second and third parts of Table I. In the limit $\Delta_c = 0$, there are 40-fold, 70-fold, and 10-fold degenerate states with energy $3U - 9J_H$, $3U - 6J_H$, and $3U - 2J_H$ respectively. On the other hand, when $J_H = 0$, there are 20-fold, 60-fold, 36-fold, and 4-fold degenerate states with energy $3U$, $3U + \Delta_c$, $3U + 2\Delta_c$ and $3U + 3\Delta_c$ respectively, depending on the number of electrons in e_g orbitals.

For finite Δ_c and J_H, d^3 spectrum as a function of Δ_c/J_H is obtained numerically as shown in Fig. 3(a). With any finite

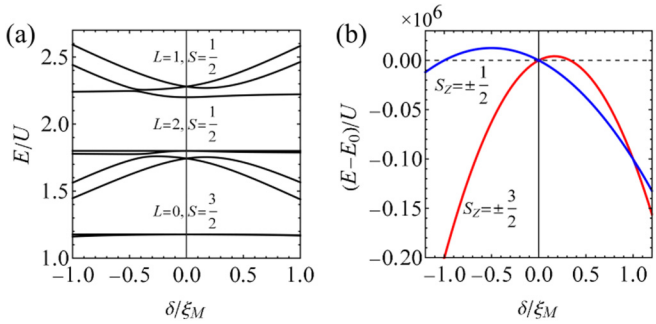

FIG. 2. (a) Spectrum of t_{2g} with $J = 0.2U$, $\xi_M = 0.15U$. ξ_M is enlarged to enlarge the splittings. (b) Lowest states with $\xi_M = 0.01U$. See also [26].

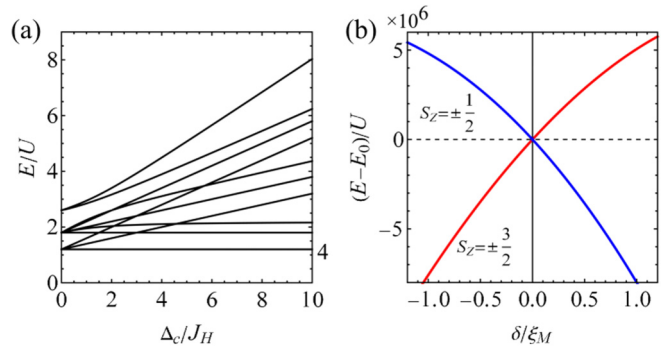

FIG. 3. (a) Spectrum of d^3 without SOC and trigonal distortions. The fourfold degeneracy of the lowest states is labeled. (b) Splitting of d^3 lowest states. We set $J_H = 0.2U$, $\Delta_c = 0.3U$, $\xi_M = 0.01U$.

Δ_c, 40-fold degenerate states split and the lowest states are given by fourfold S = 3/2 states as expected.

Similar to the above discussion, including SOC and trigonal distortions can also lead to couplings between S = 3/2 states and higher states, leading to splittings of the S = 3/2 quadruplets as shown in Fig. 3(b) for a given ratio of $\Delta_c/U = 0.3$ and $J_H/U = 0.2$. The splitting between $S_Z = \pm\frac{3}{2}$ and $S_z = \pm\frac{1}{2}$ is larger than t_{2g}^3 case, while the tendency of having $S_Z = \pm\frac{1}{2}$ for positive δ is also found without crossing around $\xi_M \sim \delta$. The larger splitting in d^3 than t_{2g}^3 indicates that e_g orbitals in excited states are important and their contribution dominates the SIA strength. Furthermore, for a positive δ, $S_z = \pm\frac{1}{2}$ is always lower in energy, implying the easy-plane SIA. Below we will perform the strong coupling perturbation theory to obtain the analytic expressions of the SIA in two cases, t_{2g}^3 and d^3.

III. ANALYTICAL DERIVATION OF SINGLE ION ANISOTROPY

Based on symmetry, the low-energy effective spin model for S = 3/2 using the octahedra coordinate system $x - y - z$ is given by [21]

$$H_{\text{spin}} = \sum_{\langle ij\rangle\in\alpha\beta(\gamma)} J\mathbf{S}_i\cdot\mathbf{S}_j + KS_i^\gamma S_j^\gamma + \Gamma\left(S_i^\alpha S_j^\beta + S_i^\beta S_j^\alpha\right) + \Gamma'\left(S_i^\alpha S_j^\gamma + S_i^\beta S_j^\gamma + S_i^\gamma S_j^\alpha + S_i^\gamma S_j^\beta\right) + A(\mathbf{S}_i\cdot\hat{Z})^2. \quad (5)$$

Among them, it was shown that Γ is absent up to the fourth order perturbation term, while Γ' is introduced by the trigonal distortion. Here in this paper we focus on the SIA term (last term) of the above spin model. S_i^Z is the spin component at site i along Z, see Fig. 1(b). The coefficient $A > 0$ corresponds to easy-plane and $A < 0$ easy-axis. In Sec. II, we have shown how the energy spectra split due to the trigonal and SOC numerically. In this section, we derive analytically the expression of A by using strong-coupling perturbation theory [21]. Both $\mathbf{l}_i\cdot\mathbf{s}_i$ and $\mathbf{L}\cdot\mathbf{S}$ SOC schemes are considered.

To derive the spin model, we start from eigenstates of $H_0 = H_{\text{Coulomb}} + H_{\text{cubic}}$ and treat H_{SOC} and H_{trig} as perturbation $V \equiv H_{\text{SOC}} + H_{\text{trig}}$. The total Hamiltonian can be written

in the subspace of lowest states of S = 3/2 and the subspace of excited states as follows:

$$H = \begin{pmatrix} H_0 & \\ & H_1 \end{pmatrix} + \begin{pmatrix} V_{00} & V_{01} \\ V_{10} & V_{11} \end{pmatrix}, \tag{6}$$

where the subscripts 0 and 1 refers to the lowest and excited states, respectively. Using downfold technique, an effective Hamiltonian is then given by

$$H_{\text{eff}} = H_0 + V_{01}\frac{1}{E_0 - H_1 - V_{11}}V_{10}. \tag{7}$$

When $\min(E_0 - H_1)$ is greater than V_{11}, we can further expand the fraction as

$$\frac{1}{E_0 - H_1 - V_{11}} = \frac{1}{E_0 - H_1} + \frac{1}{E_0 - H_1}V_{11}\frac{1}{E_0 - H_1} + ... \tag{8}$$

Below we show the results of SIA for different limits.

A. t_{2g}^3 when $\Delta_c \to \infty$

Without e_g orbitals, the eigenspace of H_0 and its energy spectra are listed in Table I where 4, 10, and 6-dimensional subspaces are classified by L and S within the LS coupling scheme. The total Hamiltonian in these 4, 10, and 6 degenerate basis is written as

$$H = \begin{pmatrix} 0 & & \\ & 3J_H & \\ & & 5J_H \end{pmatrix} + \begin{pmatrix} 0_{4\times4} & 0_{4\times10} & 0_{4\times6} \\ 0_{10\times4} & H'_{11}(\lambda) & H'_{12}(\delta) \\ 0_{6\times4} & H'_{21}(\delta) & H'_{22}(\lambda) \end{pmatrix}, \tag{9}$$

where from the perturbation part, we find that the fourfold lowest states are decoupled from the excited states. Thus the SIA under LS coupling is zero as expected due to the quenched angular momentum in t_{2g}^3.

Beyond the LS coupling, consider the SOC given by $\xi_M \sum_i \mathbf{l}_i \cdot \mathbf{s}_i$, the perturbation part is

$$H' = \begin{pmatrix} 0_{4\times4} & 0_{4\times10} & H'_{02}(\xi_M) \\ 0_{10\times4} & 0_{10\times10} & H'_{12}(\xi_M, \delta) \\ H'_{20}(\xi_M) & H'_{21}(\xi_M, \delta) & 0_{6\times6} \end{pmatrix}. \tag{10}$$

The dependence of trigonal distortion is the same as Eq. (9) as we write the Hamiltonian in the same basis. However, contrary to Eq. (9), ξ_M dependent H'_{02} and H'_{12} are nonzero. $H'_{02}(\xi_M)$ connects the lowest fourfold subspace with the excited states. This matrix structure indicates that the SIA under $\mathbf{l}_i \cdot \mathbf{s}_i$ coupling is finite.

We find that up to fourth order perturbation theory, the SIA is given by

$$A_M(t_{2g}^3) = \frac{\delta\xi_M^2(\xi_M - \delta)}{25J_H^3}. \tag{11}$$

The subscript M indicates that the SIA is induced by the SOC of the M site. The sign of $A_M(t_{2g}^3)$ is determined by the sign of δ and the relative strength of δ and ξ_M. This behavior is consistent with the numerical result shown in Fig. 2(b) where the sign change of A_M occurs around $\delta \sim \xi_M$. The difference between these two SOC schemes is due to the fact that the LS coupling is an approximation of $\mathbf{l}_i \cdot \mathbf{s}_i$ by treating the SOC between the LS subspaces as a perturbation and keeping only the diagonal elements with the lowest order [27].

TABLE II. Analytical expression for SIA.

	$\lambda L \cdot S$	$\xi_M \mathbf{l}_i \cdot \mathbf{s}_i$
t_{2g}^3	0	$\frac{\delta\xi_M^2(\xi_M - \delta)}{25J_H^3}$
d^3	$\frac{6\delta\lambda^2}{\Delta_c^2}$	$\frac{2}{3}\delta\xi_M^2\left(\frac{1}{\Delta_c^2} - \frac{1}{(\Delta_c+3J_H)^2} - \frac{6}{(10\Delta_c+21J_H)^2}\right)$

B. d^3 including e_g orbitals

As shown in Sec. III, when the e_g orbitals are included, the spectrum of d^3 is significantly different from t_{2g}^3. The spectrum of d^3 is rather complicated with the presence of both Hund's coupling J_H and cubic CFS Δ_c. We obtained the expression of SIA in the 120-dimensional d^3 space by the similar method described in the last subsection. We find that within the LS coupling scheme, the SIA is given by

$$A_M^{LS} = \frac{6\delta\lambda^2}{\Delta_c^2}. \tag{12}$$

On the other hand, using the $\xi_M \sum_i \mathbf{l}_i \cdot \mathbf{s}_i$ coupling, SIA is found as

$$A_M = \tfrac{2}{3}\delta\xi_M^2\left(\frac{1}{\Delta_c^2} - \frac{1}{(\Delta_c + 3J_H)^2} - \frac{6}{(10\Delta_c + 21J_H)^2}\right). \tag{13}$$

There are several implications. Firstly, it is well known [27] that the relation between coefficient of λ of $\mathbf{L} \cdot \mathbf{S}$ coupling and coefficient ξ_M of $\mathbf{l}_i \cdot \mathbf{s}_i$ is $\lambda = \pm\xi_M/(2S)$ with positive corresponding to less than half-filled and negative for more than half filled. According to the above relation, $\lambda = \xi_M/3$ for d^3 configuration. Substituting this relation into Eq. (12), we find it is exactly the first term of Eq. (13), while the second and third terms are beyond the LS scheme.

Secondly, we notice that the dominant contribution to SIA in Eq. (13) is the first term, which originates from the excitations to e_g orbitals. The details can be found in Appendix C. The Hund's coupling gives negative corrections, reducing the SIA strength. When J_H becomes tiny, A_M becomes negative. However, the local moment of S = 3/2 requires a finite J_H and we expect the positive A_M favoring $S_Z = \pm\frac{1}{2}$ when δ is positive.

Lastly, comparing with the SIA of the t_{2g}^3 case where a finite SIA occurs at the fourth order [see Eq. (11)], the SIA for d^3 is a third order term. Thus the contribution from e_g orbitals dominate the SIA strength. This is consistent with the numerical results of the energy splittings between $S_Z = \pm\frac{3}{2}$ and $S_Z = \pm\frac{1}{2}$ shown in Fig. 2(b) and Fig. 3(b). Also the linear dependence of δ is consistent with Fig. 3(b). For compression (positive δ), the SIA from the combination of SOC and trigonal distortion at magnetic site always prefer easy-plane anisotropy.

The SIA for t_{2g}^3 and d^3 under different SOC coupling schemes is summarized in Table II. These are shown to the lowest order of SIA for each case.

The summary shown in Table II indicates that the SOC at magnetic sites with positive trigonal distortion leads to an easy-plane (positive A) SIA. On the other hand, several MX_3 reports easy-axis (negative A) SIA, which should come from

beyond the on-site contribution to SIA. Below we investigate the contributions from the anions via hopping processes.

C. Contributions from anion SOC

Aside from the above on-site contribution to the SIA, the SOC on anions also contributes to SIA through distortion induced hoppings [21]. A rigorous derivation of A should include full processes including hopping between M and X sites involving charge configurations such as d^4p^5. For simplicity, here we use an effective hopping model derived from integrating out the hopping to anions. Up to linear order of distortion induced hoppings, we found the SIA is given by

$$A_X = -\left(\frac{4}{5J_H} + \frac{16}{5(10\Delta_c + 21J_H)}\right)\frac{t_A}{t_\pi}t_{\text{eff}}^2 + \frac{6J_H}{\Delta_c(\Delta_c + 3J_H)}\frac{t_\sigma(t_\pi t_B + t_\sigma t_C)}{t_\pi^3}t_{\text{eff}}^2 \qquad (14)$$

where the subscript X indicates SIA induced by SOC on an X site. The effective hopping is given by $t_{\text{eff}} = \frac{2t_\pi^2}{3}(\frac{1}{\Delta_{pd}-\frac{\xi_X}{2}} - \frac{1}{\Delta_{pd}+\xi_X})$.

The distortion-induced hoppings are parameterized as shown in the Appendix D and $t_A = -2\delta t_1 + \delta t_2 + \delta t_3 + \delta t_4 + \delta t_5$ and $t_B = \frac{1}{\sqrt{3}}(\delta\tau_1 + 2\delta\tau_2 - \sqrt{3}\delta\tau_3)$ as well as $t_C = \delta t_6 + \delta t_7$.

IV. APPLICATION TO CrX_3 WITH X = Cl AND I

Here we apply our theory to $3d^3$ CrX_3, since SOC and trigonal distortion are smaller than other energy scales. To determine all necessary parameters such as Δ_c, δ, and hopping parameters, we perform density functional theory (DFT) calculations. DFT calculations are performed with Vienna *ab initio* Simulation Package (VASP) [28] without the Coulomb interaction and SOC. The projector augmented wave (PAW) [29] potential and Perdew-Burke-Ernzerhof (PBE) [30] exchange-correlation functional are used. The experimental structures [31–33] are fully relaxed with SOC and various values of Hubbard U ranging from 0 eV to 4 eV until the force on each atom is less than 0.01 eV/Å. We find the structures for different U values are very similar. In the following discussion, we use the relaxed structure with U= 4 eV as an example. For both the relaxation and static calculation, we use an energy cutoff of 350 eV and a $7 \times 7 \times 7$ k-point mesh. The tight-binding parameters are obtained from Wannier90 code [34]. The Wannier parameters are listed in Appendix D The atomic SOC parameters within DFT without correlations are computed using the SOC matrix elements of a single atom in a 20 Å × 20 Å × 20Å box by OPENMX [35,36]. The atomic SOC for Cr, Cl, Br, and I are 31 meV, 82 meV, 326 meV, and 646 meV, respectively.

Table III shows the effective δ and Δ_c from the Wannier model after downfolding into the d orbitals. Since the cubic and trigonal crystal field splittings strongly depend on the $p-d$ hybridization and the underlying lattice structures, we first relax the bulk CrX_3 structures. The values listed in Table III are then obtained within LDA using the relaxed structures without U and J_H. The trend from X = Cl to I is clear. While Δ_c and δ decrease, ξ_X increases. It is important to note that δ changes sign for CrI_3 after downfolding, indicating the importance of $p-d$ hybridization (before the downfolding it is positive like Cl and Br; see the Appendix D for details). This means that both A_M and A_X are negative for the I case, leading to easy-axis anisotropy, while for Cl and Br, the opposite contributions to SIA from A_M and A_X occur.

TABLE III. DFT parameters in meV. Δ_c and δ are obtained from the Wannier model with d orbitals, which takes into account p-orbital hybridization. Δ_{pd} is obtained from the pd Wannier model.

	Δ_{pd}	Δ_c	δ	ξ_X
$CrCl_3$	2851	1481	2.45	82
$CrBr_3$	2476	1329	0.80	326
CrI_3	2080	1169	–0.96	646

Since the M and X site SOC may have opposite contributions and their strength can be enhanced by the electron-electron correlations [19,37,38], we leave ξ_M and ξ_X as two variables, and plot the SIA strength A_M as a function of ξ_M and similarly A_X as a function of ξ_X for $CrCl_3$ and CrI_3 for a fixed $J_H = 1$ eV as shown in Fig. 4. We find A_X being negative for both, while A_M is positive for $CrCl_3$ but negative for CrI_3. The sign change in A_M in CrI_3 is due to the sign change of δ via $p-d$ hybridization as mentioned above.

Experiments [39,40] reported that $CrCl_3$ has moments lying in the plane, while CrI_3 has moments out of plane [33,41]. Given that the calculated A_M is not large enough to

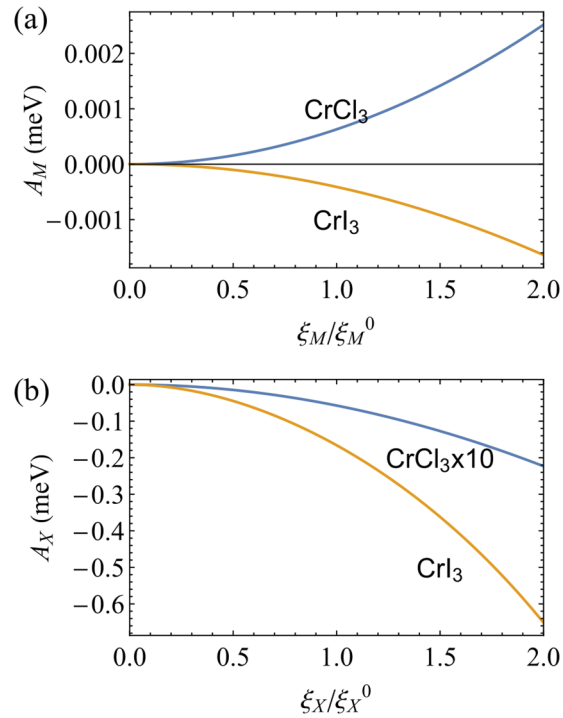

FIG. 4. SIA arises (a) from M-site SOC A_M given by Eq. (13) and (b) from X-site SOC A_X given by Eq. (14) with respect to the relative SOC strength. J_H is chosen to be 1 eV. They are both quadratic in SOC. The sign difference in A_M for both materials is due to the sign difference in total effective trigonal field δ given in Table III.

compensate A_X for $CrCl_3$, we speculate that the effective SOC at M site could be further enhanced by electron-electron correlations [19,37,38], which remains for a future study. On the other hand, for CrI_3 due to the negative sign of δ, the total SIA from both A_M and A_X is always negative leading to the easy-axis anisotropy. Quantifying the trigonal field strength is a challenging task, as it depends on the details of p- and d-orbital hybridization and corresponding charge densities. We note that the current paper does not aim to offer precise values of SIA in CrX_3, but to provide the understanding of the SIA originated from the different combinations of SOC and trigonal field in d^3 systems.

V. DISCUSSION AND SUMMARY

The existence of ferromagnetic LRO in two-dimensional (2D) systems with higher transition temperature T_c has attracted intense studies. To achieve a higher T_c in ideal 2D materials, it is essential to have a certain magnetic anisotropy that opens up a spin gap, which allows the system to avoid quantum fluctuations and set up a LRO at finite temperature. Thus understanding a microscopic origin of magnetic anisotropy in two-dimensional single-layer will guide ways to move towards a higher T_c. While the full analysis of factors that determines T_c is beyond the scope of the current study, as it requires a higher stiffness not only a finite spin gap, our study will offer valuable inputs to the current efforts of enhancing T_c.

In summary, we have studied a microscopic route to the SIA for S=3/2 in d^3 Mott insulator starting from the Kanamori-Hubbard interaction including Hund's coupling, and take into account the CFS, SOC, and trigonal distortion. We found that e_g orbitals contribution is essential to understand the SIA strength and that the tendency towards easy-plane versus easy-axis is determined by two contributions denoted by A_M and A_X. For compressed trigonal distortion, the SOC at the magnetic sites can choose either easy-plane or easy-axis depending on the sign of δ. When $\delta > 0$, it prefers the easy-plane, while $\delta < 0$ easy-axis. The sign of δ is determined by the metal-ligand hybridization, and we found that for $CrCl_3$, it takes a positive value, while for CrI_3, it is negative leading to the easy-axis anisotropy. On the other hand, for A_X, it prefers the easy-axis for both Cr trihalides.

Since we have used both SOC and trigonal distortion smaller than Hund's coupling, this theory is more applicable to $3d^3$ than $5d^3$ systems, where $J_{\text{eff}} = 3/2$ may be a better starting point than $S = 3/2$ spin states. Recent papers [42–44] of $5d^3$ have shown that in these systems there is a large spin gap. We propose that this may be relevant to the atomic SOC discussed in this paper. However cubic materials have very little distortions, implying possible bond-dependent interactions generated by SOC. Extending the current theory to the stronger SOC may explain the anisotropy observed in these systems, which is a project for future studies.

ACKNOWLEDGMENTS

This work was supported by the Natural Sciences and Engineering Research Council of Canada and the Canada Research Chairs Program. This research was enabled in part by support provided by Sharcnet and Compute Canada. Computations were performed on the GPC and Niagara supercomputers at the SciNet HPC Consortium. SciNet is funded by: the Canada Foundation for Innovation under the auspices of Compute Canada; the Government of Ontario; Ontario Research Fund - Research Excellence; and the University of Toronto.

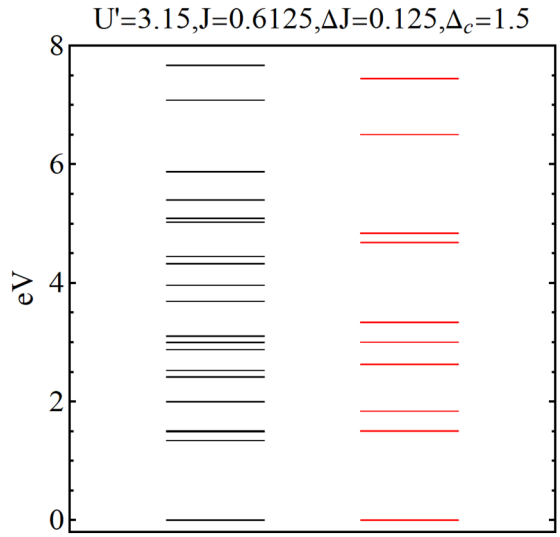

FIG. 5. Spectrum of 3 electrons on 5-d orbitals using both full interaction Hamiltonian including 3- and 4-orbital effects (black, see Eqs. 2 and 20 of [24]) and simplified multi-orbital Hamiltonian [red, see Eq. (2)].

APPENDIX A: COULOMB INTERACTION WITH 3- AND 4-ORBITAL EFFECT

To include the missing 3- and 4-orbital interaction terms, we compared our Eq. (2) with Eq. (20) of [24]. We find by setting $\Delta J = 0$, the latter reduces to the former. The spectra of 3-electron many-body states for both cases are compared in Fig. 5. Here we set the crystal field splitting $\Delta_c = 1.5$ eV to be consistent with our DFT results. Though they are different in high energy range, they have similar lower excited states. The energy splittings of $S_Z = \pm\frac{3}{2}$ and $S_Z = \pm\frac{1}{2}$ with and without 3- and 4-orbital interactions are compared in Fig. 6. The full form, the simplified one and the analytical result [Eq. (13)] are all very consistent with each other very well. This shows that the 3- and 4-orbital effects only have minor quantitative corrections to our results.

APPENDIX B: DOWNFOLDING

The perturbation process in Sec. III can also be written in another way of infinite expansion. If we write the Hamiltonian in more than two subspaces

$$H = \begin{pmatrix} H_0 & & \\ & H_1 & \\ & & \dots \end{pmatrix} + \begin{pmatrix} V_{00} & V_{01} & \dots \\ V_{10} & V_{11} & \dots \\ \dots & \dots & \dots \end{pmatrix}, \tag{B1}$$

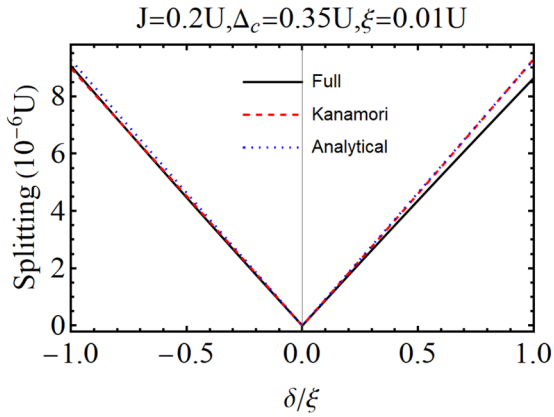

FIG. 6. Energy splitting between the $S=\pm\frac{3}{2}$ doublets and $S=\pm\frac{1}{2}$ doublets under full multi-orbital Hamiltonian and simplified Hamiltonian as well as the analytical expression from Eq. (13).

the effective Hamiltonian can be expanded as

$$\begin{aligned}H_{eff}&=\sum_i V_{0i}\frac{1}{E_0-H_i-V_{ii}}V_{i0}\\&+\sum_{i\neq j}V_{0i}\frac{1}{(E_0-H_i-V_{ii})}V_{ij}\frac{1}{(E_0-E_j-V_{jj})}V_{j0}\\&+\ldots\\&=\sum_i V_{0i}\frac{1}{E_0-H_i}V_{i0}\\&+\sum_{ij}V_{0i}\frac{1}{(E_0-H_i)}V_{ij}\frac{1}{(E_0-H_j)}V_{j0}+\ldots\\&=\sum_{i\neq j,j\neq k}\frac{H'_{0i}H'_{ij}H'_{jk}H'_{k0}}{(E_0-E_i)(E_0-E_j)(E_0-E_k)}.\end{aligned}\tag{B2}$$

This expansion is equivalent to Eq. (7).

APPENDIX C: *A* ANALYSIS

For d^3 configuration, keeping only the excited states with energy Δ_c and $2\Delta_c$ (in other words we work in the 40-fold subspace where $\Delta_c\to 0$). The Hamiltonian is

$$H=\begin{pmatrix}0&&\\&\Delta_c&\\&&2\Delta_c\end{pmatrix}+\begin{pmatrix}0_{4\times4}&H'_{01}(\xi_M)&0_{4\times12}\\H'_{10}(\xi_M)&H'_{11}(\xi_M,\delta)&H'_{12}(\xi_M)\\0_{12\times4}&H'_{21}(\xi_M)&H'_{22}(\xi_M,\delta)\end{pmatrix}.\tag{C1}$$

Up to third-order perturbation theory, we have

$$A_c=\frac{2\delta\xi_M^2}{3\Delta_c^2}.\tag{C2}$$

This gives the first term in Eq. (13) and is dominant as discussed in the main text.

APPENDIX D: WANNIER MODELS

We have two ways of building Wannier tight-binding models. One with only the d orbitals and the other with both d and p orbitals. The former is effectively integrating out the p orbitals in the latter due to the strong $p-d$ hybridization in this material. This strong hybridization can dramatically change the cubic CFS Δ_c as well as the trigonal CFS δ as can be read out from the following parameters.

1. *d*-only wannier model

The on-site Hamiltonians are (written in sequence of $d_{x^2-y^2}$, $d_{3z^2-r^2}$, d_{yz}, d_{xz}, d_{xy} and in unit meV):

$$H^{\mathrm{CrCl_3}}=\begin{pmatrix}3790.08&0&-4.01&3.43&0.58\\0&3790.09&1.64&2.64&-4.34\\-4.01&1.64&2309.22&2.44&2.45\\3.43&2.64&2.44&2309.22&2.45\\0.58&-4.34&2.45&2.45&2309.17\end{pmatrix},\tag{D1}$$

$$H^{\mathrm{CrBr_3}}=\begin{pmatrix}3255.98&0&-8.17&9.54&-1.36\\0&3255.98&6.28&3.92&-10.27\\-8.17&6.28&1926.85&0.79&0.81\\9.54&3.92&0.79&1926.84&0.8\\-1.36&-10.27&0.81&0.8&1926.81\end{pmatrix},\tag{D2}$$

$$H^{\mathrm{CrI_3}}=\begin{pmatrix}5141.62&0&-12.43&10.31&2.12\\0&5141.61&4.72&8.38&-13.17\\-12.43&4.72&3972.61&-0.96&-0.96\\10.31&8.38&-0.96&3972.61&-0.95\\2.12&-13.17&-0.96&-0.95&3972.59\end{pmatrix}.\tag{D3}$$

The difference between diagonal terms of e_g and t_{2g} orbitals gives Δ_c listed in Table III.

2. *pd* wannier model

The Hamiltonian in this *pd* model can be written as

$$H=\begin{pmatrix}H_{\mathrm{M}}&T_{\mathrm{MX}}\\T_{\mathrm{MX}}^T&H_{\mathrm{X}}\end{pmatrix}.\tag{D4}$$

Here the H_{M} is the on-site Hamiltonian of Cr atom, H_{X} is on-site Hamiltonian of ligand atoms. T_{MX} is the hopping matrix between M site and X site. For CrX_3, the 6 ligand X atoms can be related by symmetry. We only present one of the hopping matrices T_{MX_1}, as shown in Fig. 1(b).

The hopping matrix H_{MX_1} can be parametrized as

$$T_{MX} = \begin{pmatrix} t_1 & \delta\tau_1 & \delta\tau_2 \\ -t_2 & \delta\tau_3 & \delta\tau_4 \\ \delta t_1 & \delta t_2 & \delta t_3 \\ \delta t_4 & \delta t_6 & t_{a0} \\ \delta t_5 & t_{b0} & \delta t_7 \end{pmatrix}. \tag{D5}$$

This is written in the basis of d orbitals with sequence d_{x^2}, d_{z^2}, d_{yz}, d_{xz}, d_{xy}, and p orbitals with sequence p_x, p_y, p_z. The hoppings starting with δ are distortion induced hoppings and should be zero for an ideal octahedron.

From Wannier90 calculation, we have

$$H_{\mathrm{M}}^{\mathrm{CrCl_3}} = \begin{pmatrix} 2262.08 & -0.02 & -11.92 & 11.61 & 0.33 \\ -0.02 & 2262.48 & 6.72 & 7.27 & -13.88 \\ -11.92 & 6.72 & 1710.62 & 15.46 & 15.14 \\ 11.61 & 7.27 & 15.46 & 1710.65 & 15.15 \\ 0.33 & -13.88 & 15.14 & 15.15 & 1710.82 \end{pmatrix}, \tag{D6}$$

$$H_{\mathrm{M}}^{\mathrm{CrBr_3}} = \begin{pmatrix} 1778.06 & 0.01 & -9.36 & 9.84 & -0.49 \\ 0.01 & 1778.36 & 6.1 & 5.27 & -11.29 \\ -9.36 & 6.1 & 1380.58 & 9.86 & 9.66 \\ 9.84 & 5.27 & 9.86 & 1380.56 & 9.65 \\ -0.49 & -11.29 & 9.66 & 9.65 & 1380.7 \end{pmatrix}, \tag{D7}$$

$$H_{\mathrm{M}}^{\mathrm{CrI_3}} = \begin{pmatrix} 3781.78 & -0.01 & -5.89 & 5.33 & 0.57 \\ -0.01 & 3781.9 & 2.84 & 3.81 & -6.57 \\ -5.89 & 2.84 & 3493.5 & 4.81 & 4.7 \\ 5.33 & 3.81 & 4.81 & 3493.51 & 4.7 \\ 0.57 & -6.57 & 4.7 & 4.7 & 3493.61 \end{pmatrix}, \tag{D8}$$

$$H_{\mathrm{X}}^{\mathrm{CrCl_3}} = \begin{pmatrix} -1140.48 & 75.56 & -15.88 \\ 75.56 & -1139.88 & -13.67 \\ -15.88 & -13.67 & -503.56 \end{pmatrix}, \tag{D9}$$

$$H_{\mathrm{X}}^{\mathrm{CrBr_3}} = \begin{pmatrix} -1095.96 & 53.85 & -13.78 \\ 53.85 & -1094.1 & -15.86 \\ -13.78 & -15.86 & -478.33 \end{pmatrix}, \tag{D10}$$

$$H_{\mathrm{X}}^{\mathrm{CrI_3}} = \begin{pmatrix} 1415.99 & 36.19 & -11.97 \\ 36.19 & 1411.57 & -9.43 \\ -11.97 & -9.43 & 1952.06 \end{pmatrix}, \tag{D11}$$

$$T_{\mathrm{MX}}^{\mathrm{CrCl_3}} = \begin{pmatrix} -1229.15 & 125.02 & -46.19 \\ 698.08 & -61.12 & 37.92 \\ 0.24 & 23.36 & -35.49 \\ -66.75 & 5.03 & 725.57 \\ 121.75 & 718.61 & 2.26 \end{pmatrix}, \tag{D12}$$

$$T_{\mathrm{MX}}^{\mathrm{CrBr_3}} = \begin{pmatrix} -1098.54 & 91.48 & -39.8 \\ 624 & -45.81 & 31.18 \\ 1.7 & 19.23 & -26.56 \\ -56.48 & 2.76 & 644.53 \\ 91.77 & 641.93 & 2.23 \end{pmatrix}, \tag{D13}$$

$$T_{\mathrm{MX}}^{\mathrm{CrI_3}} = \begin{pmatrix} -939.04 & 48.7 & -31.06 \\ 533.92 & -36.11 & 21.24 \\ 1.4 & 14.77 & -14.06 \\ -44.83 & 1.61 & 556.07 \\ 41.72 & 547.73 & 0.35 \end{pmatrix}. \tag{D14}$$

From the above parameters, we can obtain Δ_{pd}, Δ_c^0, δ^0, $t_{pd\pi}$, $t_{pd\sigma}$ as shown in Table III, and distortion induced hoppings in Eq. (D5).

[1] A. Soumyanarayanan, N. Reyren, A. Fert, and C. Panagopoulos, Emergent phenomena induced by spinorbit coupling at surfaces and interfaces, Nature (London) **539**, 509 (2016).

[2] N. Miao, B. Xu, L. Zhu, J. Zhou, and Z. Sun, 2D intrinsic ferromagnet from van der Waals antiferromagnets, J. Am. Chem. Soc. **140**, 2417 (2018).

[3] B. Huang, G. Clark, E. Navarro-Moratalla, D. R. Klein, R. Cheng, K. L. Seyler, D. Zhong, E. Schmidgall, M. A. McGuire, D. H. Cobden *et al.*, Layer-dependent ferromagnetism in a van der Waals crystal down to the monolayer limit, Nature (London) **546**, 270 (2017).

[4] C. Gong, L. Li, Z. Li, H. Ji, A. Stern, Y. Xia, T. Cao, W. Bao, C. Wang, Y. Wang *et al.*, Discovery of intrinsic ferromagnetism in two-dimensional van der Waals crystals, Nature (London) **546**, 265 (2017).

[5] B. Huang, G. Clark, D. R. Klein, D. MacNeill, E. Navarro-Moratalla, K. L. Seyler, N. Wilson, M. A. McGuire, D. H. Cobden, D. Xiao *et al.*, Electrical control of 2D magnetism in bilayer CrI^3, Nat. Nanotechnol. **13**, 544 (2018).

[6] N. Sivadas, S. Okamoto, X. Xu, C. J. Fennie, and D. Xiao, Stacking-dependent magnetism in bilayer CrI_3, Nano Lett. **18**, 7658 (2018).

[7] L. Webster and J.-A. Yan, Strain-tunable magnetic anisotropy in monolayer $CrCl_3$, $CrBr_3$, and CrI_3, Phys. Rev. B **98**, 144411 (2018).

[8] Z. Wu, J. Yu, and S. Yuan, Strain-tunable magnetic and electronic properties of monolayer CrI_3, Phys. Chem. Chem. Phys. **21**, 7750 (2019).

[9] X. Cai, T. Song, N. P. Wilson, G. Clark, M. He, X. Zhang, T. Taniguchi, K. Watanabe, W. Yao, D. Xiao *et al.*, Atomically thin $CrCl_3$: An in-plane layered antiferromagnetic insulator, Nano Lett. **19**, 3993 (2019).

[10] T. Li, S. Jiang, N. Sivadas, Z. Wang, Y. Xu, D. Weber, J. E. Goldberger, K. Watanabe, T. Taniguchi, C. J. Fennie *et al.*, Pressure-controlled interlayer magnetism in atomically thin CrI_3, Nat. Mater. **18**, 1303 (2019).

[11] N. D. Mermin and H. Wagner, Absence of Ferromagnetism or Antiferromagnetism in One- or Two-Dimensional Isotropic Heisenberg Models, Phys. Rev. Lett. **17**, 1133 (1966).

[12] J. L. Lado and J. FernÃ¡ndez-Rossier, On the origin of magnetic anisotropy in two dimensional CrI_3, 2D Mater. **4**, 035002 (2017).

[13] D.-H. Kim, K. Kim, K.-T. Ko, J. H. Seo, J. S. Kim, T.-H. Jang, Y. Kim, J.-Y. Kim, S.-W. Cheong, and J.-H. Park, Giant Magnetic Anisotropy Induced by Ligand LS Coupling in Layered Cr Compounds, Phys. Rev. Lett. **122**, 207201 (2019).

[14] C. Xu, J. Feng, H. Xiang, and L. Bellaiche, Interplay between Kitaev interaction and single ion anisotropy in ferromagnetic CrI_3 and $CrGeTe_3$ monolayers, npj Comput. Mater. **4**, 57 (2018).

[15] I. Lee, F. G. Utermohlen, D. Weber, K. Hwang, C. Zhang, J. van Tol, J. E. Goldberger, N. Trivedi, and P. C. Hammel, Fundamental Spin Interactions Underlying the Magnetic Anisotropy in the Kitaev Ferromagnet CrI_3, Phys. Rev. Lett. **124**, 017201 (2020).

[16] J. Kanamori, Electron correlation and ferromagnetism of transition metals, Prog. Theor. Phys. **30**, 275 (1963).

[17] G. Jackeli and G. Khaliullin, Mott Insulators in the Strong Spin-Orbit Coupling Limit: From Heisenberg to a Quantum Compass and Kitaev Models, Phys. Rev. Lett. **102**, 017205 (2009).

[18] J. G. Rau, E. K.-H. Lee, and H.-Y. Kee, Generic Spin Model for the Honeycomb Iridates beyond the Kitaev Limit, Phys. Rev. Lett. **112**, 077204 (2014).

[19] H.-S. Kim, Vijay Shankar V., A. Catuneanu, and H.-Y. Kee, Kitaev magnetism in honeycomb $RuCl_3$ with intermediate spin-orbit coupling, Phys. Rev. B **91**, 241110(R) (2015).

[20] P. P. Stavropoulos, D. Pereira, and H.-Y. Kee, Microscopic Mechanism for a Higher-Spin Kitaev Model, Phys. Rev. Lett. **123**, 037203 (2019).

[21] P. P. Stavropoulos, X. Liu, and H.-Y. Kee, Magnetic anisotropy in spin-3/2 with heavy ligand in honeycomb Mott insulators: Application to CrI_3, Phys. Rev. Research **3**, 013216 (2021).

[22] H. Liu, J. Chaloupka, and G. Khaliullin, Kitaev Spin Liquid in 3D Transition Metal Compounds, Phys. Rev. Lett. **125**, 047201 (2020).

[23] S. Sugano, *Multiplets of Transition-Metal Ions in Crystals* (Elsevier Science, St. Louis, 2014).

[24] M. E. A. Coury, S. L. Dudarev, W. M. C. Foulkes, A. P. Horsfield, P.-W. Ma, and J. S. Spencer, Hubbard-like Hamiltonians for interacting electrons in s, p, and d orbitals, Phys. Rev. B **93**, 075101 (2016).

[25] Y. Wang, G. Fabbris, M. Dean, and G. Kotliar, Edrixs: An open source toolkit for simulating spectra of resonant inelastic x-ray scattering, Comput. Phys. Commun. **243**, 151 (2019).

[26] H. Suzuki, H. Gretarsson, H. Ishikawa, K. Ueda, Z. Yang, H. Liu, H. Kim, D. Kukusta, A. Yaresko, M. Minola *et al.*, Spin waves and spin-state transitions in a ruthenate high-temperature antiferromagnet, Nat. Mater. **18**, 563 (2019).

[27] P. Fazekas, *Lecture Notes on Electron Correlation and Magnetism* (World Scientific, Singapore, 1999).

[28] G. Kresse and J. Hafner, *Abinitio* molecular dynamics for liquid metals, Phys. Rev. B **47**, 558 (1993).

[29] P. E. Blöchl, Projector augmented-wave method, Phys. Rev. B **50**, 17953 (1994).

[30] J. P. Perdew, K. Burke, and M. Ernzerhof, Generalized Gradient Approximation Made Simple, Phys. Rev. Lett. **77**, 3865 (1996).

[31] B. Morosin and A. Narath, X ray diffraction and nuclear quadrupole resonance studies of chromium trichloride, J. Chem. Phys. **40**, 1958 (1964).

[32] H. Braekken, Die Kristallstruktur von Chromtribromid, Kongelige Norske Videnskapers Selskab, Forhandlinger **5**, 42 (1932).

[33] M. A. McGuire, H. Dixit, V. R. Cooper, and B. C. Sales, Coupling of crystal structure and magnetism in the layered, ferromagnetic insulator CrI_3, Chem. Mater. **27**, 612 (2015).

[34] G. Pizzi, V. Vitale, R. Arita, S. Blügel, F. Freimuth, G. Géranton, M. Gibertini, D. Gresch, C. Johnson, T. Koretsune, Wannier90 as a community code: New features and applications, J. Phys.: Condens. Matter **32**, 165902 (2020).

[35] T. Ozaki, Variationally optimized atomic orbitals for large-scale electronic structures, Phys. Rev. B **67**, 155108 (2003).

[36] T. Ozaki and H. Kino, Numerical atomic basis orbitals from H to Kr, Phys. Rev. B **69**, 195113 (2004).

[37] H. Isobe and N. Nagaosa, Enhancement of spin-orbit interaction by competition between Hund's coupling and electron hopping, J. Phys.: Conf. Ser. **592**, 012058 (2015).

[38] A. Tamai, M. Zingl, E. Rozbicki, E. Cappelli, S. RiccÃ², A. de la Torre, S. McKeown Walker, F. Bruno, P. King, W. Meevasana, M. Shi, M. Radovi, N. Plumb, A. Gibbs, A. Mackenzie, C. Berthod, H. Strand, M. Kim, A. Georges, and F. Baumberger, High-Resolution Photoemission on Sr_2RuO_4 Reveals Correlation-Enhanced Effective Spin-Orbit Coupling and Dominantly Local Self-Energies, Phys. Rev. X **9**, 021048 (2019).

[39] J. Cable, M. Wilkinson, and E. Wollan, Neutron diffraction investigation of antiferromagnetism in $CrCl_3$, J. Phys. Chem. Solids **19**, 29 (1961).

[40] M. A. McGuire, G. Clark, Santosh KC, W. M. Chance, G. E. Jellison, V. R. Cooper, X. Xu, and B. C. Sales, Magnetic behavior and spin-lattice coupling in cleavable van der Waals layered $CrCl_3$ crystals, Phys. Rev. Materials **1**, 014001 (2017).

[41] J. F. Dillon and C. E. Olson, Magnetization, resonance, and optical properties of the ferromagnet CrI_3, J. Appl. Phys. **36**, 1259 (1965).

[42] D. I. Badrtdinov, L. Ding, C. Ritter, J. Hembacher, N. Ahmed, Y. Skourski, and A. A. Tsirlin, MoP_3SiO_{11}: A $4d^3$ honeycomb antiferromagnet with disconnected octahedra, Phys. Rev. B **104**, 094428 (2021).

[43] D. D. Maharaj, G. Sala, C. A. Marjerrison, M. B. Stone, J. E. Greedan, and B. D. Gaulin, Spin gaps in the ordered states of La_2LiXO_6(X=Ru, Os) and their relation to the distortion of the cubic double perovskite structure in $4d^3$ and $5d^3$ magnets, Phys. Rev. B **98**, 104434 (2018).

[44] E. Kermarrec, C. A. Marjerrison, C. M. Thompson, D. D. Maharaj, K. Levin, S. Kroeker, G. E. Granroth, R. Flacau, Z. Yamani, J. E. Greedan, and B. D. Gaulin, Frustrated fcc antiferromagnet Ba_2YOsO_6: Structural characterization, magnetic properties, and neutron scattering studies, Phys. Rev. B **91**, 075133 (2015).